Journal of Thermal Analysis and Calorimetry (2025) 150:22651–22665
https://doi.org/10.1007/s10973-025-15131-6

Investigation of the mechanic, thermal, and electrochemical corrosion behavior of Fe effect on IN718 produced by PM used in the aviation industry

Muhammed Enes İlgazi[1,2] · Esra Balci[2] · Sercan Basit[3] · Fethi Dağdelen[4] · İlven Mutlu[5]

Received: 18 March 2025 / Accepted: 23 November 2025 / Published online: 9 December 2025

Abstract
This study examined the microstructure, thermal oxidation behavior, electrical conductivity, microhardness, and corrosion behavior of Ni–Cr–Mo–Nb–Fe superalloys, depending on the Ni and Fe ratio change. When the high-temperature oxidation behaviors of the alloys were examined, it was seen that the activation energy (E_o) required for oxidation raised as the Ni ratio increased. The activation energy values were compared, and it was determined that the highest sample was PM10, 133 kJ mol^{-1}. The oxide layers formed by the alloy elements are clearly visible in the images obtained as a result of SEM analysis. EDX peaks and results show the composition of the alloy and the presence of metal oxide compounds. It was found that the microhardness value increased when the mass ratio of Fe element was reduced and the mass ratio of Ni element reached the highest value (PM10). With the increase in addition rates of nickel, the electrical conductivity of super alloys raised. According to the C_R results of the samples, PM10 exhibited a relatively high passive current density indicating a faster dissolution rate and its corrosion resistance was calculated to be significantly lower than the other samples. The analysis determined that the sample with the highest corrosion resistance was PM8. As a result, it is noteworthy that it can be used in the aviation and space industry, especially at high temperatures, due to its good resistance to corrosion.

Keywords Oxidation · Corrosion · Superalloy · Aircraft material · Microstructure

Introduction

Superalloys represent distinctive multi-constituent metallic systems that exhibit exceptional mechanical characteristics, especially under elevated temperatures [1]. Indeed, the ability of superalloys to endure extended loading at temperatures approaching their melting points is intricately associated with their remarkable creep resistance [2]. Furthermore, considerable resistance to both corrosion and oxidation under severe operational conditions render superalloys viable candidates for a variety of specialized applications [3]. Inconel alloys demonstrate remarkable mechanical strength, particularly through the mechanisms of precipitation hardening and solid solution hardening. In this regard, a salient characteristic of Inconel alloys is the precipitation hardening mechanism, wherein strengthening phases such as γ' and γ'' are generated [4]. The ordered crystalline structure of these phases increases the necessary energy by constraining the mobility of dislocations, thereby enhancing the overall strength of the material [5]. Additionally, the microstructure may exhibit the presence of metal carbides [4, 6, 7], needle-like δ phase [4, 6, 7], and closely packed hexagonal Laves phase [4, 6, 7].

Generally, the strategic incorporation of alloying elements plays a pivotal role in governing the high-temperature strength of Inconel alloys by influencing both the microstructure [8–10] and the resultant phases formed [8–10]. Among the principal Inconel alloys, Inconel 718 is particularly

✉ Fethi Dağdelen
fdagdelen@firat.edu.tr

1 Department of Metallurgical and Materials Engineering, Yildiz Technical University, 34220 Istanbul, Turkey

2 Department of Aircraft Maintenance and Repair, Istanbul Nisantasi University, 34398 Istanbul, Turkey

3 Department of Mechanical Engineering, Kirşehir Ahi Evran University, 40100 Kirsehir, Turkey

4 Faculty of Science, Department of Physics, Firat University, 23119 Elazig, Turkey

5 Department of Metallurgical and Materials Engineering, Istanbul University-Cerrahpasa, l34320 Istanbul, Turkey

well-suited for applications exposed to severe carburizing and oxidizing environments [6, 11]; Inconel 625 exhibits exceptional strength and corrosion resistance over a wide temperature range (− 150 to + 1000 °C) [12, 13]; Inconel 738LC demonstrates remarkable high-temperature strength together with improved castability [4]; and Inconel 939, a relatively recent alloy, is distinguished by its microstructural stability and oxidation-resistant weldability [14, 15]. These nickel-based alloys are characterized by their superior fatigue resistance, radiation resilience, oxidation, and corrosion resistance, in addition to their capacity to sustain these mechanical and physical properties at elevated temperatures [4, 16]. In recent years, the most extensively utilized and widely investigated high-temperature nickel-based superalloy has been Inconel 718 [17–19]. Nickel-based superalloys are extensively utilized in applications such as superchargers, gas turbines, jet propulsion systems, fastening components, afterburners, and turbine wheels [20]. These alloys are predominantly selected for their performance in corrosive environments, including sulfuric acid, chlorine, and favorable hydrogen service conditions [21]. The manufacturing process of nickel-based superalloys significantly influences the final product's quality and defects [22]. Investment casting is a prevalent technique for fabricating these components [23]. Modifications in the manufacturing process and alloying elements can enhance properties and minimize defects [24]. Consequently, minor alterations in alloy compositions can yield substantial effects [25]. Casting-produced superalloys may encounter defects, including shrinkage defects, hot cracks, and porosity, impacting product quality [26]. Key production techniques for nickel-based superalloys consist of investment casting, powder metallurgy (PM), additive manufacturing (AM), and hot isostatic pressing (HIP) [27]. Notably, powder metallurgy offers benefits such as uniform alloy structures, reduced waste, and the fabrication of high-performance components [28]. Furthermore, it allows for the production of intricately shaped parts and facilitates controlled heat treatments to optimize material characteristics [29, 30]. Masaya Higashi et al. examine the impact of initial powder particle size on the hot workability of nickel-based superalloys. Increased particle size correlates with reduced oxygen content and precursor particle boundary (PPB) density, enhancing hot workability. Fine powder samples exhibit a higher susceptibility to cavitation and crack initiation due to elevated PPB density. Optimal hot workability is observed at γ' sub-solvus temperatures (approximately 1100 °C). The findings indicate that larger particles yield superior mechanical properties, contrasting with the general preference for fine powders in superalloy production [31]. Yin-long Shao et al. analyzed the impact of Ti and Al on the microstructure and elemental distribution in nickel-based powder metallurgy superalloys. The findings indicated that Ti and Al preferentially localized in the γ' phase, leading to the formation of $\gamma+\gamma'$ structures at grain boundaries and promoting γ' phase growth. Furthermore, increasing Ti and Al concentrations enhanced the distribution of Cr, Co, and Mo within the γ matrix. These observations imply that precise control of Ti and Al contents is essential for optimizing the mechanical properties of superalloys [32]. Generally, Fe is frequently regarded as a crucial matrix element possessing the capability to partially substitute for nickel, represented by Ni, to a certain degree in various alloy compositions. To attain the optimal level of machinability while simultaneously minimizing production costs, significant quantities of iron elements are strategically incorporated into the formulation of some innovative superalloys, thereby effectively replacing the nickel element in these advanced materials [33]. Nevertheless, it is worth noting that certain methodologies associated with powder metallurgy, including pressing-sintering process as well as metal injection molding, present significant advantages in terms of achieving near-net-shape forming, thereby facilitating the efficient production of aviation engine components that closely resemble the final desired geometries, which can lead to reductions in material waste and potentially enhance the overall performance characteristics of the manufactured parts [34, 35]. In this regard, it is clearly obvious that further experimental studies are needed to contribute to the optimization of this methodology.

To our knowledge, no prior studies have systematically explored deliberate Fe → Ni substitution in Inconel 718 via powder metallurgy. Conventional IN718 alloys have relatively fixed Fe (~ 18 mass%) and Ni (~ 50–55 mass%) by specification [36], so composition variations are normally incidental (e.g., dilution during welding or cladding). The only analogous work is in related Ni-alloys or surface coatings. For example, Wu et al. varied Fe content (by intentional dilution) in Inconel 625 laser-cladding layers and found that exceeding ~ 5 mass% Fe sharply degraded corrosion resistance [36]. This highlights Fe's sensitivity, but 625 lack the γ''/γ' phases of 718. Similarly, Fe-substitution studies exist in Co–Ni systems (e.g., Ni–Co–Fe superalloys) where replacing Ni with Fe affects γ' volume and creep properties, but these do not address IN718's chemistry or powder routes. Other works (e.g., on alloy X-750) note that higher Fe improved water-side corrosion by forming trevorite [37], yet these occur in cast or wrought materials under high-temperature water—again differing from our PM 718 case.

This study presents cost-effective, durable materials with Fe addition for high-temperature and corrosion-resistant aviation engine components. It addresses a research gap by analyzing superalloys produced by powder metallurgy compared to alloys produced by other methods and the effect of Fe addition on the material structure. The research elucidates how substituting nickel with Fe alters the mechanical and electrochemical properties of superalloys. Consequently, it

yields valuable insights for developing optimized, economical, high-performance materials in aviation and future academic investigations.

Material method

In this investigation, specimens of a nickel-based superalloy were synthesized utilizing fine powders of Ni, Cr, Mo, Nb, and Fe through the process of press-sintering. Table 1 presents the chemical compositions and coding of the samples. The powder mixtures were mechanically alloyed by ball milling using ZrO_2 ceramic balls (3 mm in diameter) at a rotational speed of 400 rpm for approximately 6 h. The duration of mechanical alloying of 6 h proved adequate for achieving homogenization of these alloys. The ratio of metal powder to balls was set to 1/10. Polyvinyl alcohol (PVA) was employed as a binder to enhance green strength before the sintering process (Merck, Germany). Following the mechanical alloying phase, a PVA solution comprising 6 mass percent was incorporated into the metal powder. This PVA solution consisted of 3 mass percent PVA mixed with distilled water. The metal powder was manually blended with the PVA solution. Subsequently, the powder-binder mixtures were subjected to compaction at a pressure of 350 MPa. The height of the cylindrical samples was approximately 16–18 mm, while the diameter of the samples was 10–12 mm. In Fig. 1, the sintering procedure involves raising the temperature to 390 °C (thermal decomposition) with a heating rate of 6 °C/min and a holding time of 30 min, followed by an increase to sintering temperatures at a rate of 10 °C min^{-1}. The thermal debinding temperature of the polyvinyl alcohol (PVA) was determined to be approximately 390 °C through the application of thermogravimetric analysis (TGA, SDT Q600). The PVA present in the green specimens underwent thermal elimination as an integral component of the sintering cycle. The green specimens were subjected to sintering at 1200 °C for 60 min within a vacuum environment in a horizontal tube furnace (MTI, USA).

The properties of electrical conductivity are significant, as its values are influenced by both the chemical composition and the microstructural characteristics of materials. Measurements of conductivity serve as a means for the examination of various heat treatment processes. The electrical conductivity of the alloys was assessed utilizing the

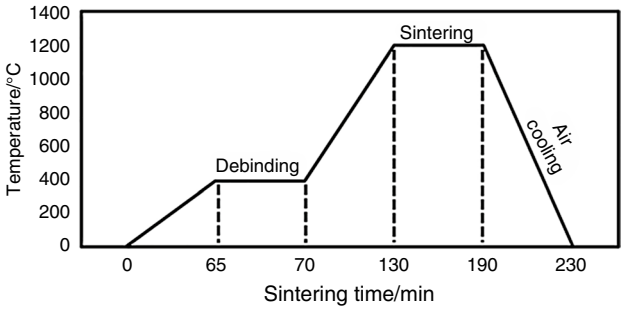

Fig. 1 Schematic diagram of the sintering process for the powder metallurgy superalloys

(WeldCheck, ETher NDE) eddy current measurement apparatus. The determination of electrical conductivity was conducted in accordance with the international annealed copper standard (IACS). The electrical conductivity of annealed copper is established as 100% IACS at a temperature of 20 °C, and consequently, the conductivity of the specimen was ascertained.

The alloys were investigated for their thermal oxidation behavior. Samples with identical dimensions ($1.2 \times 1.2 \times 0.5$ mm^3) were sectioned, and their surface roughness was removed. The specimens were then ultrasonically cleaned in alcohol and dried in hot air. Isothermal and non-isothermal oxidation experiments were carried out by Perkin Elmer Pyris TG/DTA thermal analysis system. These prepared samples were exposed to air atmosphere from room temperature (RT) to 1000 °C, and the mass gain was recorded as a function of temperature throughout the experiment. It was determined that the alloys exhibited logarithmic mass gain at high temperatures in the non-isothermal measurement. For this reason, three different temperature values in the logarithmic region (500, 700, and 900 °C) were selected to determine the isothermal mass gain. Argon gas was used to protect the samples from oxidation during heating selected at these temperatures. Then, to determine the thermal kinetic energies and thermal activation energies of the alloys, thermogravimetric (TG) mass gain curves due to 80 min isothermal oxidation at 500, 700, and 900 °C in air atmosphere were measured. Microstructural and elemental analysis measurements of the thermally oxidized alloys were taken with a scanning electron microscope-energy-dispersive X-ray spectroscopy (SEM–EDX) device.

Table 1 Sample codes and their compositions

Sample	Atomic percentage/at%					Mass percentage/mass%				
	Ni	Cr	Mo	Nb	Fe	Ni	Cr	Mo	Nb	Fe
PM8	47.08	19.354	1.798	0.928	30.892	48.0	17.5	3.0	1.5	30
PM9	52.057	19.402	1.802	0.931	25.807	53.0	17.5	3.0	1.5	25
PM10	62.192	19.500	1.812	0.935	15.562	63.0	17.5	3.0	1.5	15

The hardness evaluations of the specimens were conducted utilizing a Vickers hardness tester (Zwick Roell ZHU 1875 LKV). A total of five distinct measurements were obtained by exerting 1000 g of load and 10 s of dwell time, sampling various regions of the surface of each specimen. Subsequently, the mean values and standard deviations were computed employing statistical methodologies.

To assess the mechanical characteristics of each specimen, quasi-static cyclic compression–compression experiments were conducted utilizing a mechanical testing apparatus (Devotrans, Turkey). The elastic modulus of the specimens was ascertained after the compression testing procedure. The elastic modulus was additionally assessed via a pulse receiver-type ultrasonic apparatus (General Electric, USA). The elastic modulus was computed using the following Eq. 1, where V_T and V_L represent the transverse and longitudinal velocities, respectively, and ρ denotes density. A normal probe and a 4-MHz beam longitudinal wave transducer were utilized for the ultrasonic velocity determinations [12].

$$E = \rho V_T^2 \frac{3V_L^2 - 4V_T^2}{V_L^2 - V_T^2} \quad (1)$$

The abrasion experiments were conducted in a rotary drum abrasion tester (Devotrans, Türkiye, DVT DA 6) using a 10-N static load with and length of 20 m. The speed of the drum was set to 20 rpm.

The electrochemical potentiodynamic scanning (PDS) experiments were conducted on the samples utilizing a potentiostat/galvanostat (Interface 1000, Gamry) at ambient temperature. Before the initiation of the experiments, the samples underwent sanding to a finish of 2500 grit. The experimental procedures were executed in accordance with the three-electrode methodology within a 3.5% NaCl electrolyte volume of 500 mL. A graphite electrode and an Ag/AgCl reference electrode were employed as the counter and reference electrodes, respectively. The variations in open circuit potential (OCP) for the stabilization of the alloy surfaces of about 7200 s in the presence of electrolytes were recorded before the execution of the potentiodynamic scanning (PDS) tests. Following the establishment of equilibrium, the scanning commenced on the alloys from a value of − 0.7 V relative to the OCP and proceeded anodically at a scan rate of 1 mV·s^{-1}.

Results and discussion

To find the temperature on the oxidation kinetics of the super alloys (SA's), a TG–DTA analysis was performed in an air atmosphere from RT to 1000 °C and a heating rate of 20 °C min^{-1}. Non-isothermal TG–DTA measurement results

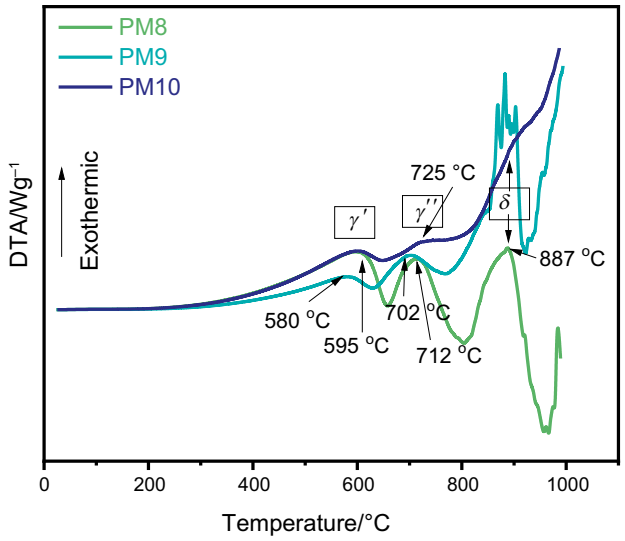

Fig. 2 The results determined from DTA curves of the alloys

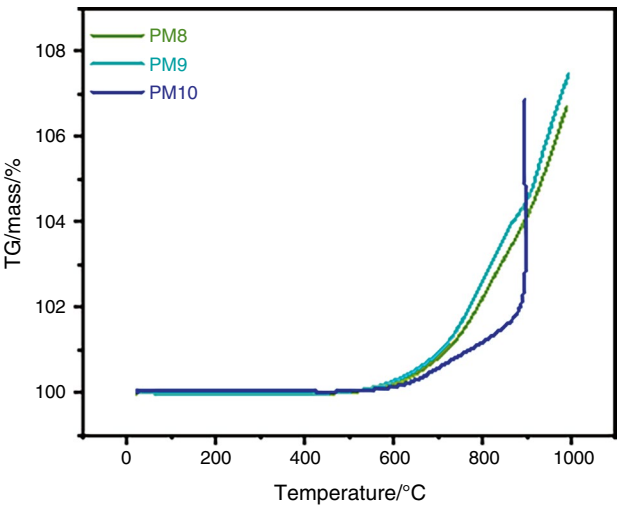

Fig. 3 The thermogravimetric mass gains of the alloys

are given in Fig. 2 and 3, respectively. In the DTA results in Fig. 2, the phase change graph of the alloys at high temperatures is given. As can be seen, three exothermic peaks can be observed in the heating ramp and are indicated with arrows. These exothermic peaks are associated with the γ′, γ″, δ precipitations [34]. While the γ′ precipitation phase occurred at 595 °C in PM8 and PM10, it occurred at 580 °C in PM9. The γ″ precipitations were formed in PM 8, PM 9, and PM 10 at 712, 702, and 725 °C, respectively. Finally, the δ precipitations occurred at approximately 887 °C in all three samples. These results are consistent with the literature [34, 38]. According to Fig. 3, the non-isothermal oxidation curves of alloys can be divided into two stages. At the beginning of the oxidation test, the mass gain increases linearly because of

passive oxide layer formation; this stage is referred to as linear oxidation [39]. A parabolic mass increase occurred in all three samples after approximately 500 °C. It was observed that the mass surface oxidation rate in the PM10 sample was higher at 900 °C. According to these results, the chosen oxidation temperatures of our study fit parabolic oxidation laws. Non-isothermal oxidation behaviors were determined for each sample at temperatures selected from the parabolic region of 500, 700, and 900 °C for 80 min. The percentage mass increase of the samples with time is given in Fig. 4. As shown in Fig. 5, the mass increase of each sample is the highest at 900 ℃. That is, the oxidation rate of alloys is higher at high temperatures. It is also observed that the reaction rate in alloys decreases with increasing time. The oxidation constant rate k_p, can be expressed by the following Eq. 2 [40, 41]:

$$\left(\Delta W/\Delta A\right)^2 = k_p\, t \tag{2}$$

where $(\Delta W/A)$ is the mass gain per unit area of a specimen, t is the oxidation time. k_p can be calculated from the slope of linear regression line on $(\Delta W/A)^2$ versus t plot (Fig. 5). These values calculated for 500, 700, and 900 °C are shown in Table 2. According to k_p values and oxidation temperature, oxidation activation energy can be calculated by the following Eq. 3:

$$k_p = k_o \exp\left(E_o/RT\right) \tag{3}$$

k_o is the pre-exponential constant, R is the gas constant, T is the temperature. Figure 5 shows the plot of 1000/T versus $\ln k_p$ for the studied temperature range for all samples.

Another parameter that is closely related to the analysis of the crystallization behavior of alloys during phase transformations is thermal activation energy. Thermal oxidation energies (E_o) of the samples are given in Table 2. According to these results, the thermal activation energies required for the oxidation of PM8, PM9, and PM10 samples are 112.606, 123.821, and 133.578 J mol^{-1}, respectively. Additionally, this variation is given in Fig. 6. Comparison of the three alloys indicates that increasing the nickel content and decreasing the iron content leads to higher thermal oxidation activation energy. This may be due to the formation of nickel oxide compounds, NiO (nickel monoxide) and Ni_2O_3 (nickel trioxide), at high temperatures as well as the increase in the Ni ratio in the alloy. As a result, the sample with the highest activation energy value is PM10 and its value is 133 kJ mol^{-1}.

SEM images of PM8 alloy subjected to air oxidation from room temperature (RT) to 1000 °C and isothermally oxidized at 500, 700, and 900 °C are given in Fig. 7. The oxide layers formed by the alloying elements are clearly visible. As a result of keeping this alloy isothermally in air at 500 °C

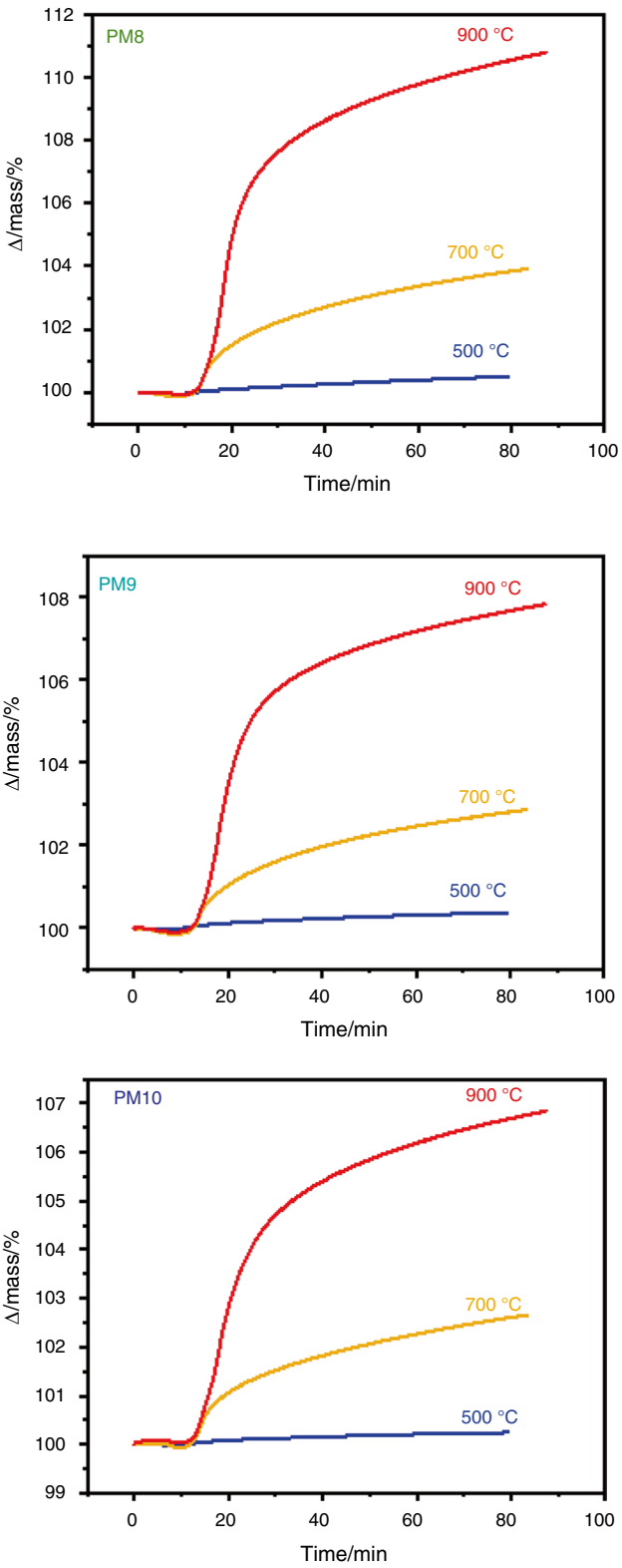

Fig. 4 Mass gain of superalloys during 80 min oxidation at a non-isothermal temperature of 500–900 °C

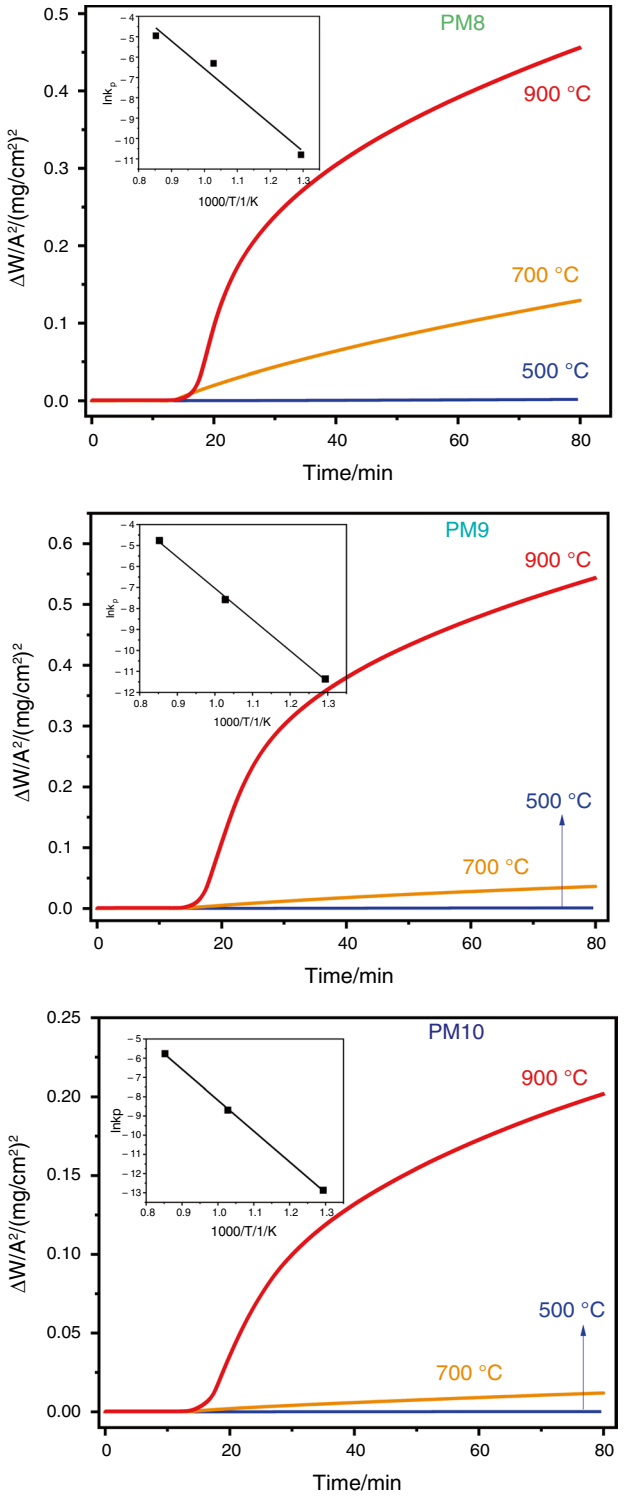

Fig. 5 $(\Delta W/A)^2$ according to time, and k_p according to 1000/T graphs to calculate thermal activation energies

for 80 min., a capillary nano-oxide layer was formed on its surfaces. As the isothermal temperature increases, i.e., at 700 °C, the nano-oxide rods increase and become thicker. At 900 °C, these oxide rods are seen to cover the entire surface as an oxide layer. To explain the surface compositions of the alloys subjected to isothermal surface oxidation at 900 °C, mapped SEM and EDX results are given in Fig. 8–10. SEM and mapped SEM images are given in Fig. 8a and c. EDX peaks and analysis results taken from the entire surface are given in Fig. 8b and d. As shown in Fig. 8b, the oxide components of the Ni element are dominant. It can be said that these regions are nickel monoxide. There are iron oxide compounds in some places on the surface. The most well-known oxides of iron are hematite, also called alpha iron oxide (α-Fe_2O_3), magnetite also known as gamma iron oxide (γ-Fe_2O_3), and magnetite (Fe_3O_4). The high-temperature oxide compound of iron is γ-Fe_2O_3, which has weak ferromagnetic properties. In Fig. 9a–d, the isothermal oxidized SEM–EDX and mapped SEM images of PM9 alloy at 900 °C are given. Although iron oxide structures are predominant on the alloy surface, nickel oxide structures are also present (Fig. 9b). EDX peaks and results show the composition of the alloy and the presence of metal oxide compounds (Fig. 9c, d). Similarly, the SEM–EDX and mapped SEM image of the PM10 sample isothermally oxidized at 900 °C are given in Fig. 10a–d.

The average of microhardness values taken from five different regions was taken. The standard deviations of the results obtained were also calculated and are given in Fig. 11. When looking at the microhardness results, PM10 alloy appears to have the highest microhardness value. It can be said that this result is due to the increase in the nickel ratio in the alloy.

The understanding of mechanical properties, including Young's modulus E and hardness, is essential for designing components under various loads. Quasi-static cyclic compression tests and ultrasonic methods were utilized to analyze the mechanical properties of the samples. The ultrasonic method is advantageous due to its non-destructive nature and high accuracy [42]. In Fig. 12, the elastic modulus values obtained from compression tests were recorded as 199 GPa for PM8, 200 GPa for PM9, and 203 GPa for PM10. The ultrasonic method measurements of 203 GPa for PM8, 204 GPa for PM9, and 206 GPa for PM10. Both methodologies indicated that PM10 exhibited the highest elastic modulus. PM10 also demonstrated a more ductile behavior relative to the other samples. In an investigation, it has been observed that a reduction in the iron content present within the alloy may result in significant alterations to both the microstructural characteristics and the distribution of various phases within the material. More specifically, the intentional diminishment of iron levels can facilitate the stabilization of hardening phases, such as γ'' (Ni_3Nb), which play a crucial role in enhancing the mechanical properties of the alloy [43]. Extensive research has demonstrated that the presence of

Table 2 The oxidation constant rate and activation energy of the alloys

Sample names	Oxidation temperature/℃	k_p/μg mm^{-2} s^{-1}	lnk_p/μg mm^{-2} s^{-1}	Activation energy/J mol^{-1}
PM8	500	2.05×10^{-5}	– 10.797	112.606
	700	1.82×10^{-3}	– 6.309	
	900	7.06×10^{-3}	– 4.953	
PM9	500	1.17×10^{-5}	– 11.359	123.821
	700	5.13×10^{-4}	– 7.576	
	900	8.53×10^{-3}	– 4.764	
PM10	500	2.56×10^{-6}	– 12.871	133.578
	700	1.67×10^{-4}	– 8.696	
	900	3.12×10^{-3}	– 5.770	

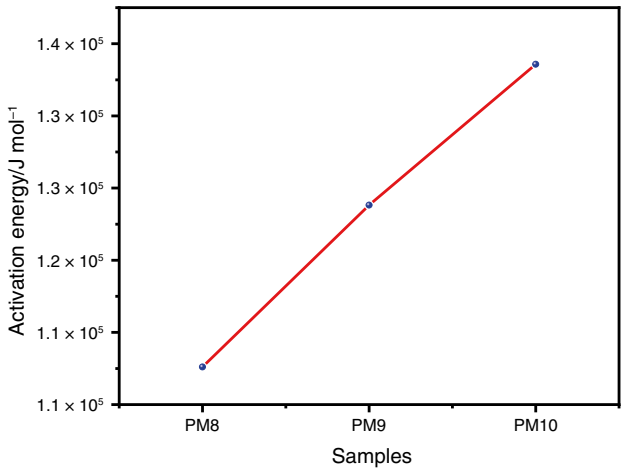

Fig. 6 Activation energy graphs required for thermal oxidation of alloys

these hardening phases is instrumental in promoting an increase in the elastic modulus, as they effectively inhibit the movement of dislocations and concurrently strengthen the interatomic bonds within the material's structure [44].

In Fig. 13, a stationary cylindrical superalloy specimen is systematically lowered to apply a specific pressure against the abrasive fabric affixed to the surface of the cylindrical drum. The abrasive influence resulting from the friction on the specimen arises from its lateral displacement across the abrasive fabric at a defined angle, while the drum is in rotation. The quantification of mass loss from the specimen is subsequently conducted. A relative index of abrasion resistance can effectively describe the degree of abrasion resistance exhibited. The ARI (% Index of abrasion resistance) values are determined to be 0.5 for PM8, 0.4 for PM9, and 0.3 for PM10. A lower value of the abrasion resistance index signifies diminished abrasion resistance. In Fig. 11, if the hardness values show an increasing trend while the fractured hard phases fail to demonstrate adequate adhesion on the surface, it is plausible that the wear rate may escalate as a consequence of the hard abrasive particles [45].

In an investigation, it was elucidated that within a material undergoing continuous and sliding wear deformation, microstructural features resembling arrows were generated in the solid solution regions, oriented perpendicular to the direction of sliding. This observed microstructural configuration was posited to be definitive evidence of plastic deformation occurring within the material throughout the wear testing process. The ultimate manifestation of this wear is characterized by the presence of abrasive grooves within nickel superalloys [46, 47].

In a separate study, it becomes evident that the regions occupied by the fractured Ni_3Nb and Ni_3Mo intermetallic phases, which are presumed to form as a result of surface wear in the superalloys, are distinctly delineated and subsequently subjected to pronounced plowing. The absence of fracture lines at the interface between the intermetallic phase and the matrix phase (solid solution) following the wear experiment provides compelling evidence that this interface exhibits a high degree of adhesion. In the investigations conducted, the lack of fractures at the interface between the intermetallic phase and the matrix phase (solid solution) post-wear testing stands as irrefutable proof of the significant adhesion properties of this interface [47].

Figure 14 illustrates results of electrical conductivity test of superalloys. With the increase in addition rates of nickel, the electrical conductivity of super alloys raised. While the electrical conductivity of PM8 superalloy was measured as 1.60%IACS, the effects of replacing the element iron with nickel increased electrical conductivity. Electrical conductivity measurements of PM9 and PM10 samples were measured as 1.62 and 1.80%IACS, respectively. Although Ni and Fe possess the same number of nominal conduction electrons (two) [48], the electronic transport behavior in Ni-rich matrices is governed not merely by free-electron count but by changes in electron-scattering mechanisms and band-structure effects. In metallic alloys, electrical resistivity arises from the cumulative contribution of various

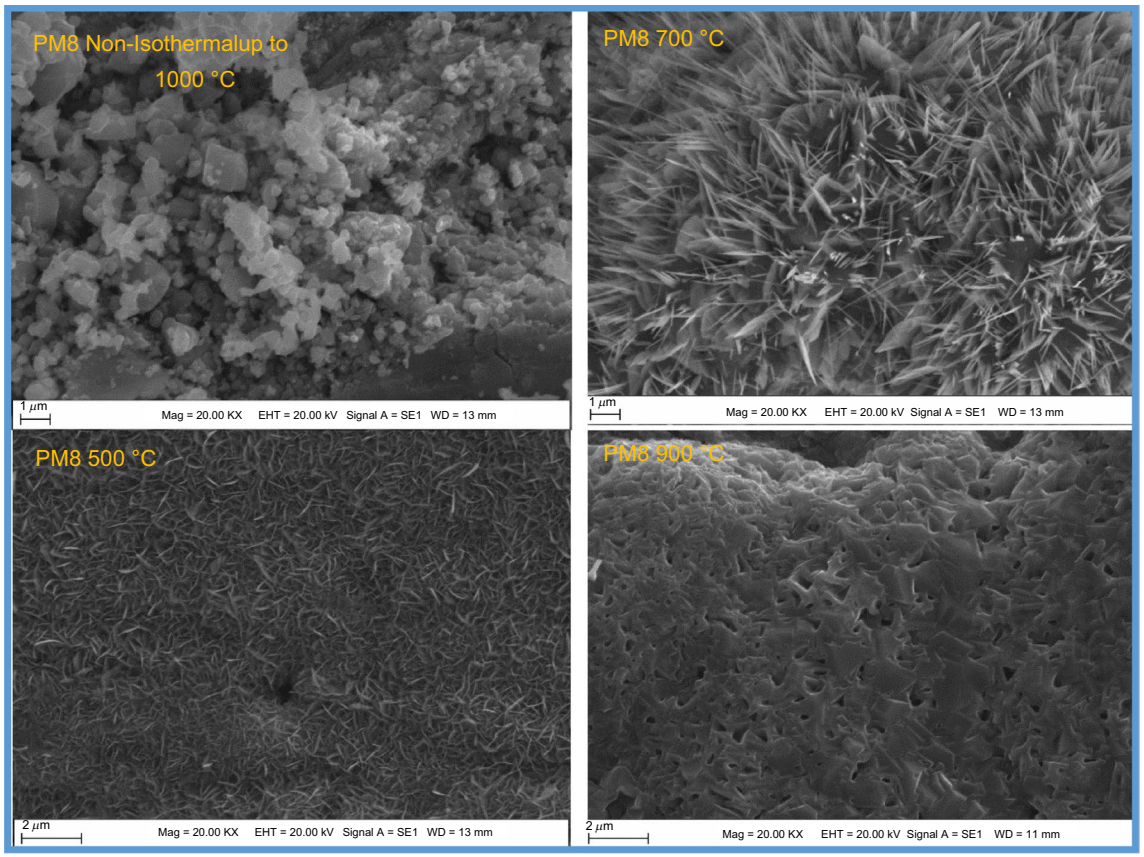

Fig. 7 SEM images of alloys oxidized at specific temperature

scattering sources—phonons, solute atoms, dislocations, and precipitates—as described by Matthiessen's rule (each scattering mechanism adds independently to the total resistivity) [49, 50].

In Ni–Fe alloys, the small increase in conductivity with higher Ni content can be associated with the markedly low residual resistivity characteristic of these systems. Ferromagnetic Ni and Fe form a majority-spin conduction channel, which reduces scattering in this spin band and provides a "short-circuit" pathway for electrons, resulting in inherently higher conductivity in Ni-rich matrices compared with Fe-rich compositions [51]. As the Ni fraction increases, the electronic density of states and band curvature for the majority-spin electrons change in a way that lowers resistivity relative to Fe, in agreement with prior studies on Ni–Fe solid solutions.

Moreover, the relative contributions of solute-atom scattering must be considered. Each alloying element introduced into the γ-matrix acts as a scattering center, lowering conductivity through local lattice distortions and electronic potential fluctuations [52]. When Fe is replaced by Ni—an element with a more compatible atomic radius and electronic structure with the Ni-based γ-matrix—the overall solute-scattering contribution is reduced. Thus, increasing Ni content effectively decreases the concentration of higher-scattering solute species (e.g., Fe, Nb, Ti), which leads to higher measured conductivity. The relationship between the resistivity of the γ phase and the concentration of solute atoms can be expressed by the following equation [52].

$$\rho_\gamma = \rho_0 + \rho_{\text{imp}} = \rho_0 + x_{\text{imp}} \frac{\Delta\rho_{\text{imp}}}{a} \tag{4}$$

In this expression, ρ_0 denotes the intrinsic resistivity of the alloy matrix in the absence of solute atoms, ρ_{imp} represents the resistivity contribution arising from solute atoms in solid solution, x_{imp} is the atomic fraction of the solute species, and $\frac{\Delta\rho_{imp}}{a}$ corresponds to the resistivity increment associated with a single solute atom. This formulation demonstrates that the resistivity of the γ phase increases proportionally with solute concentration.

Another essential factor is matrix purification via precipitation reactions. In Ni-base superalloys, elements such as Nb, Ti, and Al tend to form ordered γ' ($Ni_3(Al,Ti)$) or γ'' (Ni_3Nb) phases during thermal exposure. Although precipitates themselves may scatter electrons, their formation removes solute atoms from the matrix, thereby reducing impurity scattering in the γ-phase. Numerous studies have

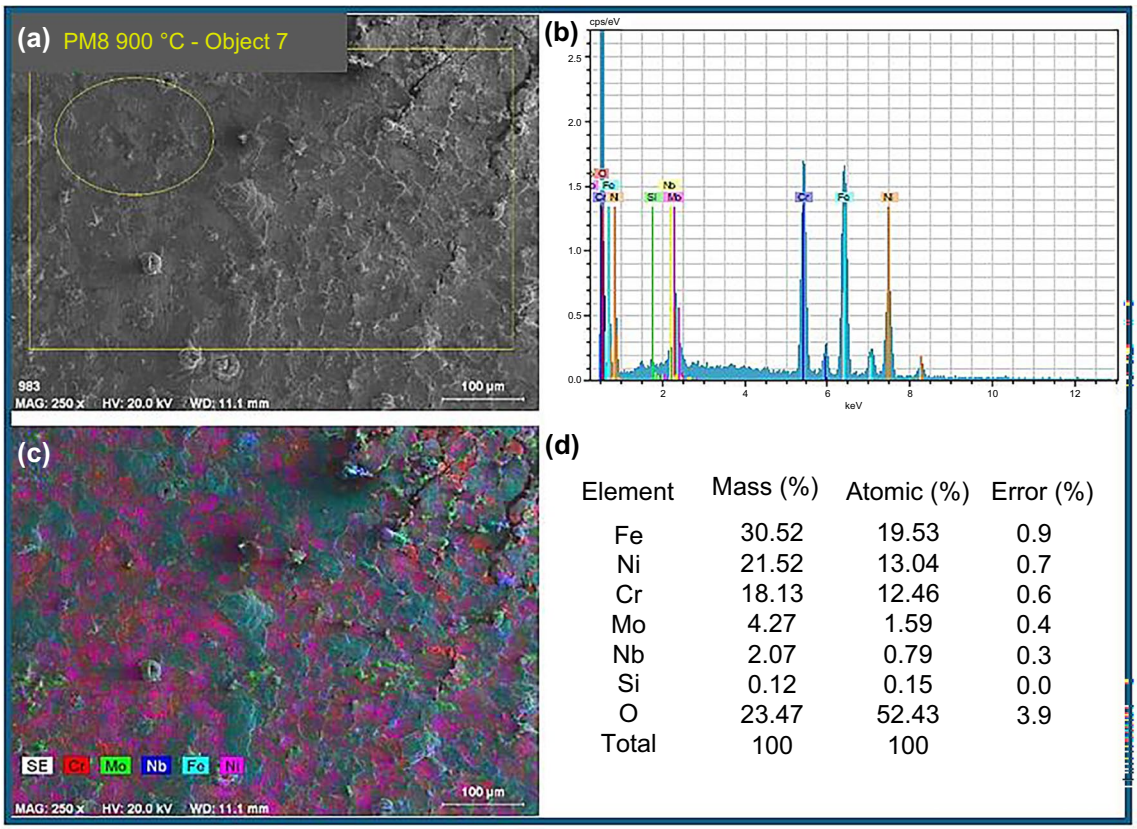

Element	Mass (%)	Atomic (%)	Error (%)
Fe	30.52	19.53	0.9
Ni	21.52	13.04	0.7
Cr	18.13	12.46	0.6
Mo	4.27	1.59	0.4
Nb	2.07	0.79	0.3
Si	0.12	0.15	0.0
O	23.47	52.43	3.9
Total	100	100	

Fig. 8 **a** SEM, **b** EDX, **c** mapping, and **d** elemental analysis images of PM8 alloy

shown that this "purification" effect can dominate, resulting in increased conductivity even when the precipitate fraction rises [53–55]. In the present Ni–Cr–Fe–Nb–Mo alloys, matrix purification is primarily governed by γ'' (Ni_3Nb) precipitation, since the absence of Al and Ti prevents the formation of γ'-type ordering. During aging, Nb partitions into γ'' precipitates, decreasing its concentration in the γ-matrix. As Nb is among the strongest electron-scattering solutes in Ni-based matrices, this depletion significantly lowers impurity scattering, thereby enhancing electrical conductivity a behavior consistent with prior reports on IN718 aging kinetics and resistivity evolution. For instance, Nagarajan et al. [55] demonstrated that aging of Inconel 718 increases electrical conductivity because the removal of Nb from the γ-matrix (into γ'') markedly decreases solute-atom scattering despite the presence of additional precipitates.

In the present alloys, substitution of Fe with Ni not only reduces the concentration of Fe—an element that contributes more strongly to solute-scattering in a Ni-rich matrix—but can also influence the stability of γ'/γ'' precipitation. A Ni-rich matrix is less prone to forming Fe-containing intermetallic phases, thereby lowering the likelihood of additional scattering sources. Consequently, both decreased residual solute scattering and increased matrix-purification effects contribute to the observed enhancement in electrical conductivity as Ni content increases.

After analyzing the structural and mechanical properties of the superalloys (SAs), their corrosion behavior was also investigated. In all kinds of industrial applications, especially in the aviation and space industries, materials must be carefully selected according to their areas of use so that they can adapt to the corrosive environment without causing undesirable chemical reactions. Corrosion is the process of metals and their alloys entering a corrosive environment and causing their chemical structures to deteriorate or change. In this study, the purpose of taking corrosion measurements based on electrochemical analysis is based on the principle of providing basic information about the corrosion resistance of materials in NaCl. Additionally, some parameters related to EIS methods were determined. Potentiodynamic measurements were carried out using electrochemical methods to determine the corrosion rates of the prepared samples. Tafel curves of samples analyzed at room temperature are given in Fig. 15a. The corrosion rate (C_R) obtained as a result of the analysis was calculated for a one-year estimate using Eq. 5 [56]:

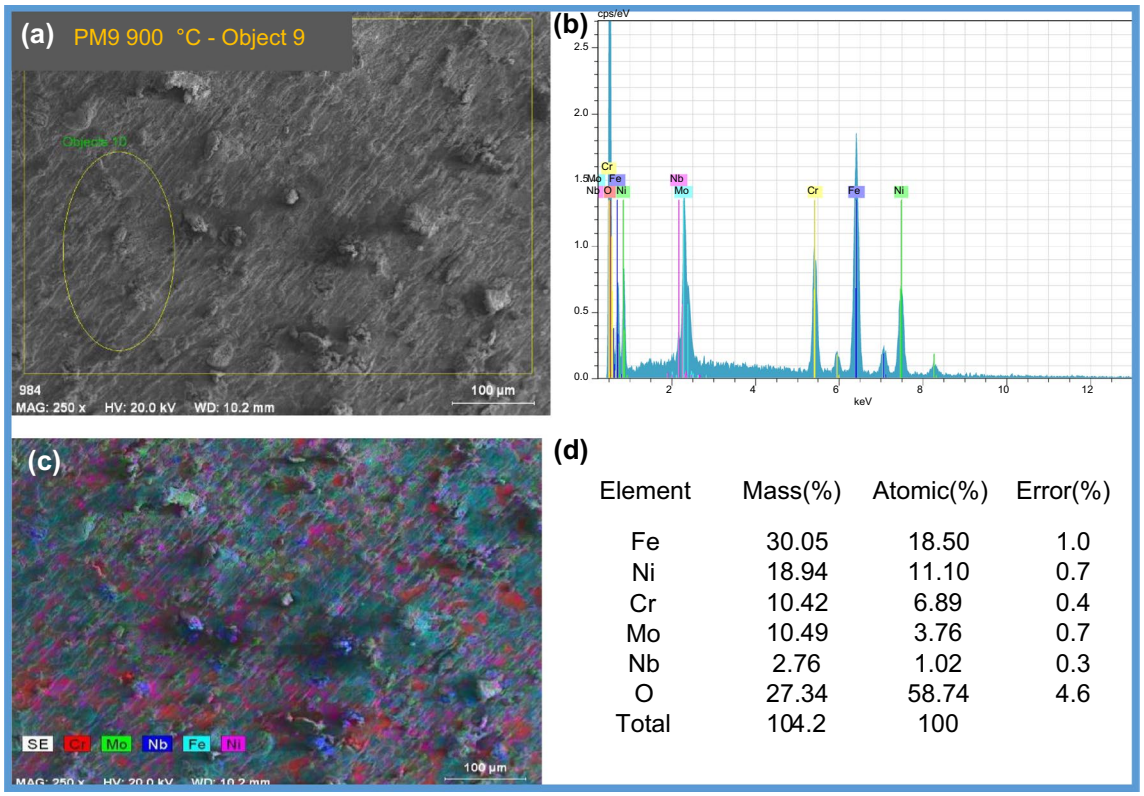

Element	Mass(%)	Atomic(%)	Error(%)
Fe	30.05	18.50	1.0
Ni	18.94	11.10	0.7
Cr	10.42	6.89	0.4
Mo	10.49	3.76	0.7
Nb	2.76	1.02	0.3
O	27.34	58.74	4.6
Total	104.2	100	

Fig. 9 **a** SEM, **b** EDX, **c** mapping, and **d** elemental analysis images of PM9 alloy

$$\text{Corrosion rate} = \frac{0.13 \times I_{\text{corr}} \times A}{n \times D} \tag{5}$$

Here, A represents the atomic mass of the components, n represents the number of electrons transferred per single atom, and D represents the density. After finding the C_R of the samples, the corrosion resistance (Rp) was calculated by the Stern–Geary [57] Eq. 6:

$$R_p = \left(\beta_a \times \beta_c\right) / \left(I_{\text{corr}} \times \left(\beta_a + \beta_c\right) \times 2.303\right) \tag{6}$$

Corrosion parameters of the samples are given in Table 3. When Fig. 15.a was examined, all samples exhibited typical active–passive behavior. Corrosion current density and C_R represent the amount of material that has corroded over time, and the C_R of the samples (mmpy) was calculated for an estimated one-year period. According to the C_R results of the samples (Table 3), PM10 exhibited a relatively high passive current density indicating a faster dissolution rate and its corrosion resistance was calculated to be significantly lower than the other samples. It is also observed that with the increase in corrosion current density (I_{corr}), the corrosion rate of the samples increases but their corrosion resistance decreases. As a result, the analysis determined that the sample with the highest corrosion resistance was PM8 (0.083 MΩ cm^2). The obtained values were also consistent with those reported in the literature. For example, electrochemical polarization measurements of IN718 samples in 3.5% NaCl solution at room temperature under different pH conditions, conducted by T. Thuneman et al., yielded similar results (0.075 MΩ cm^2) [58]. EIS is another parameter that provides insight into the corrosion behavior of the samples. In this technique, a very low AC voltage is applied to the electrochemical cell, and the resulting current is measured. The EIS (impedance) spectra of the samples are presented in Fig. 15b. The capacitive behavior observed in the spectra suggests that the corrosion mechanism is supported by the presence of a passive film. As clearly shown in Fig. 15b, the impedances of the passive films formed on PM9 and PM10 are lower than that of PM8. This indicates that PM9 and PM10 exhibit lower corrosion resistance, whereas PM8 demonstrates the highest resistance.

Building on these electrochemical results, PM8 (with higher Fe and lower Ni content) exhibited superior corrosion resistance compared with PM10 (with lower Fe and higher Ni), which can be explained in terms of passive film chemistry and microstructural characteristics. Although higher Ni content is often expected to enhance

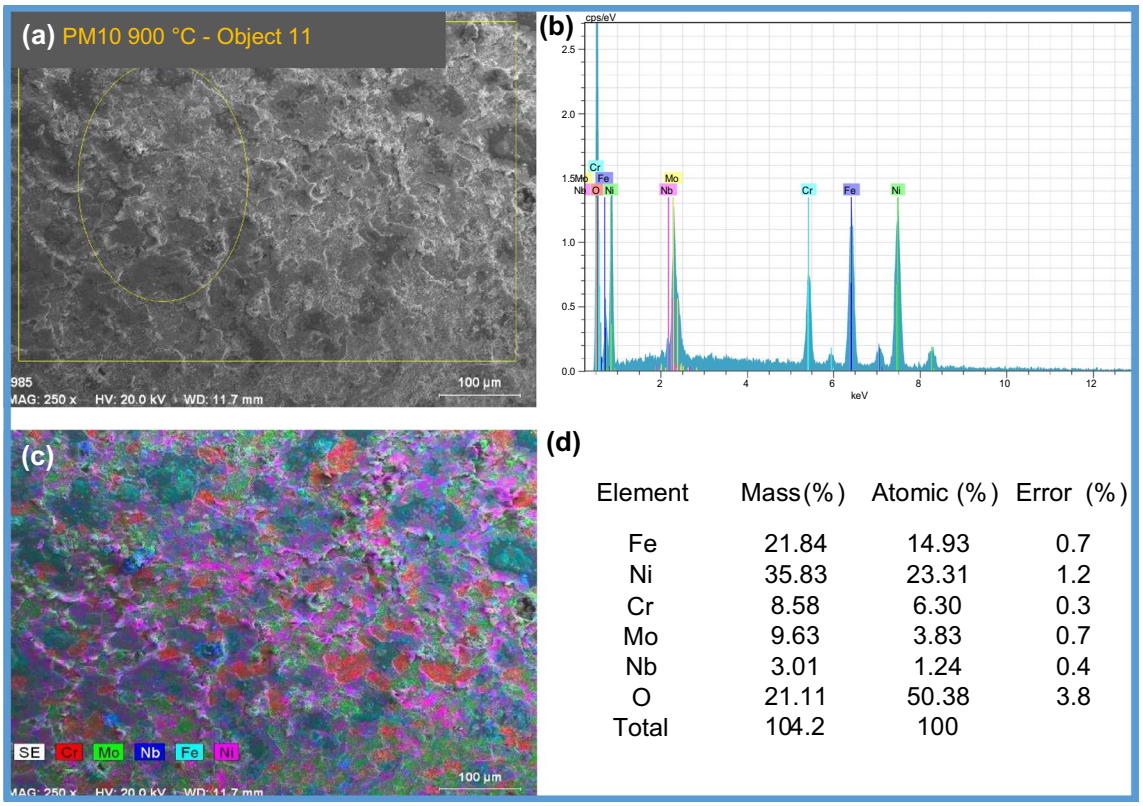

Fig. 10 (**a**) SEM, (**b**) EDX, (**c**) mapping, and (**d**) elemental analysis images of PM10 alloy

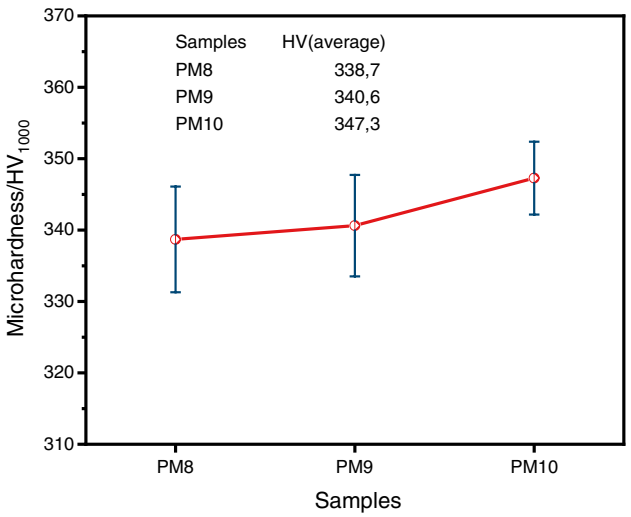

Fig. 11 Microhardness curves of alloys

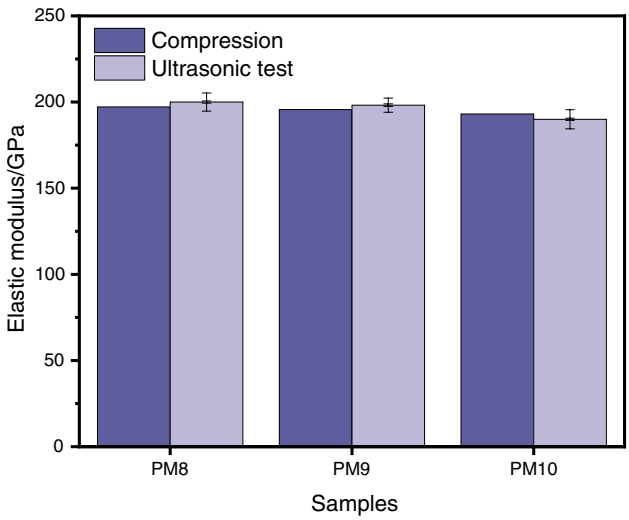

Fig. 12 Comparison of elastic modulus of AS's

corrosion resistance, our data show that the Fe-richer alloy (PM8) forms a more protective passive film in 3.5% NaCl solution. Ni–Cr superalloys typically rely on a Cr_2O_3-rich inner passive layer, while Ni or Fe species appear as spinel or hydroxide phases. In practice, Ni-based alloys generally develop a bilayer structure consisting of an inner Cr_2O_3 layer (with some $NiCr_2O_4$ spinel) and an outer layer enriched in Ni and Fe oxides [59]. Higher Fe

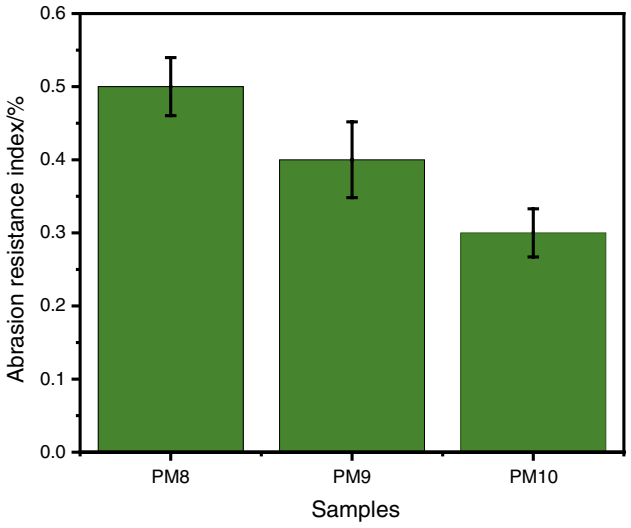

Fig. 13 Comparison of the abrasion resistance index (ARI) of various Ni-based superalloy samples

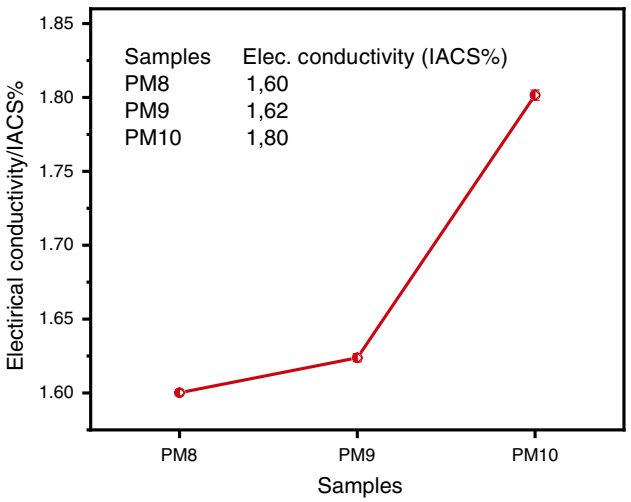

Fig. 14 Electrical conductivity measurement graphs of samples taken at RT and under constant voltage

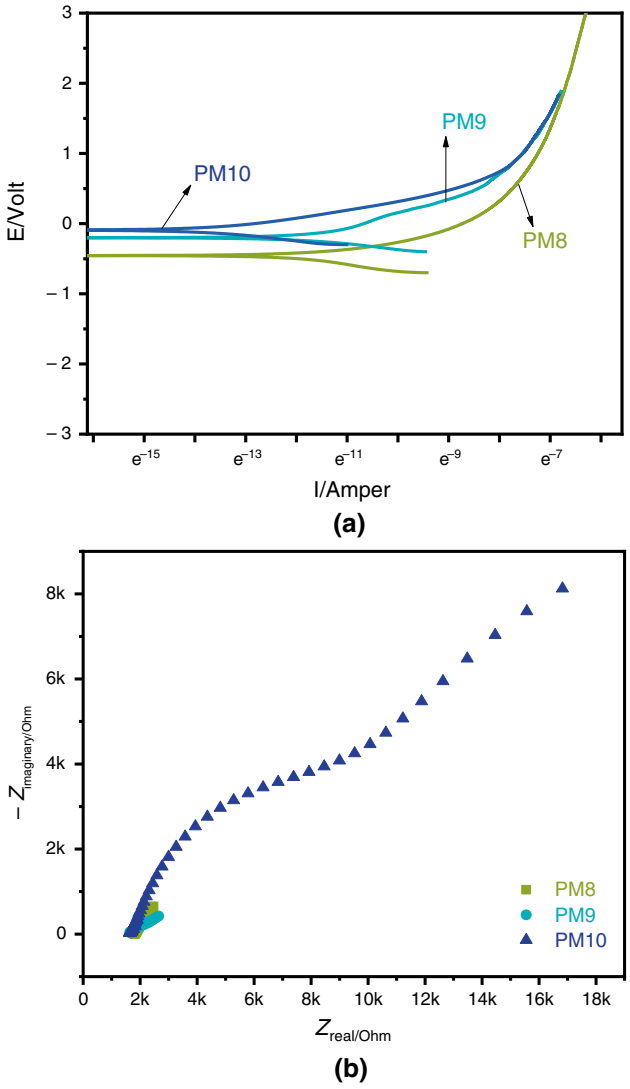

Fig. 15 (**a**) Tafel curve of the samples obtained in NaCl at RT, (**b**) The EIS or impedance spectrum of the SA's

content promotes the formation of $NiFe_2O_4$ (trevorite) spinel in the outer layer, whereas lower Fe content leads to the formation of NiO or mixed $Ni(OH)_2/Fe_2O_3$ phases. For instance, Tuzi reported that an X-750 alloy containing 8 mass% Fe forms a thick and compact $NiFe_2O_4$ outer film that significantly suppresses corrosion [37]. Another study [60] comparing different Fe contents similarly showed that relatively high Fe promotes the development of a more adherent and less porous oxide layer, despite overall similarities in oxide evolution.

In our PM alloys, the elevated Fe content of PM8 is anticipated to thermodynamically favor the incorporation of Fe into spinel-type oxides, thereby promoting the formation of $NiFe_2O_4$ and associated Ni–Fe spinels. The enrichment of these phases within the passive layer is known to improve film compactness and adhesion, ultimately yielding a more robust and protective corrosion barrier. In contrast, the lower Fe content in PM10 appears to favor the formation of NiO with limited Fe–Ni spinel contribution. Consequently, the superior corrosion resistance of PM8 can be attributed to its Fe-rich composition, which promotes the formation of a thicker mixed $NiFe_2O_4$–$NiCr_2O_4$ spinel film together with a compact underlying Cr_2O_3 layer [61].

Electrochemical analyses indicate that Fe content in IN718 significantly affects passive film formation and stability, thereby influencing corrosion resistance. The PM8 specimen, with higher Fe, exhibited more noble open circuit potentials and higher polarization resistance, reflecting a thicker and more protective Ni–Fe–Cr oxide layer. Fe also

Table 3 Electrochemical polarization parameters of the SA's in NaCl at RT

Sample	E_{corr}/V	β_a/V	β_c/V	$I_{corr}/\mu Acm^{-2}$	Corrosion rate/mmpy	Corrosion resistance Rp/MΩ cm^{-2}
PM8	– 449	138.1	197.0	422.0	4.38×10^{-2}	0.083
PM9	– 201	261.0	172.7	543.7	5.59×10^{-2}	0.082
PM10	– 0.093	161.0	144.7	674.3	6.78×10^{-2}	0.049

stabilizes γ'' and other Fe-containing precipitates, promoting uniform film formation and reducing localized dissolution, while the diminished presence of destabilizing phases such as Laves further enhances corrosion resistance. In contrast, the PM10 specimen, with lower Fe content, formed a less protective passive layer and showed comparatively lower corrosion resistance [58].

Conclusions

In this study, the effects of thermal oxidation temperature on the alloys, mechanical properties, and physical microstructures of Ni–Cr–Mo–Nb–Fe superalloys prepared with different compositions were investigated and some important results summarized below were obtained. °C

1. In the DTA results of the samples, the γ', γ'', δ phases, which are believed to correspond to the three exothermic peaks observed in the phase change graph of the alloys at high temperatures, were detected in accordance with the literature.
2. According to DT-TGA results, the oxidation temperatures selected in the study follow the parabolic oxidation laws. When comparing these three alloys in terms of activation energies, increasing the nickel content and decreasing the iron content led to an increase the thermal oxidation activation energy of the alloy.
3. When the activation energy values, which are closely related to the crystallization behavior of the samples, were compared, it was determined that the highest value was PM10, 133 kJ mol^{-1}.
4. The oxide layers formed by the alloy elements are clearly visible in the images obtained as a result of SEM analysis. As the isothermal temperature increases, i.e., at 700 ℃, the nano-oxide rods increase and become thicker. EDX peaks and results show the composition of the alloy and the presence of metal oxide compounds.
5. In NiCrMoFe alloys, the mass ratios of Cr and Mo elements were kept constant, while the mass ratios of Ni and Fe elements were changed. As a result, it was found that the microhardness value increased when the mass ratio of Fe element was reduced and the mass ratio of Ni element reached the highest value (PM10).
6. Compression and ultrasonic testing elucidate the critical role of mechanical properties, particularly Young's modulus, in the design of load-bearing components. The results reveal that PM10 exhibits a superior elastic modulus and greater ductility. Additionally, the findings indicate that decreasing the iron content in the alloy stabilizes hardening phases such as γ', which enhances material strength by inhibiting dislocation movement and strengthening interatomic bonds, thereby improving the overall mechanical properties.
7. The study elucidates differences in wear resistance among the samples. PM8 exhibited superior resistance compared to PM10. Wear rates were influenced by hardness values and the adherence of fragmented hard phases. Microstructural observations revealed plastic deformation and abrasive grooves. Notably, the fractured Ni_3Nb/Ni_3Mo intermetallic phases adhered strongly to the matrix. This strong adhesion was evidenced by the lack of interfacial fractures, confirming the material's high wear resistance.
8. With the increase in addition rates of nickel, the electrical conductivity of super alloys raised.
9. According to the C_R results of the samples, PM10 exhibited a relatively high passive current density indicating a faster dissolution rate and its corrosion resistance was calculated to be significantly lower than that of the other samples. The corrosion mechanism of capacitive behavior is considered to be supported by the passive film. As a result, it is noteworthy that it can be used in the aviation and space industry, especially at high temperatures, due to its good resistance to corrosion.

Acknowledgements This article is a part of the MSc. study of M.E. İLGAZİ. This work was also supported by the Kirsehir Ahi Evran University Scientific Research Projects Coordination Unit under project number: MMF.A3.25.007

Author contributions M.E. ILGAZI and I.MUTLU prepared the samples. E. BALCI performed the EDX-SEM tests. F. DAGDELEN performed the TG–DTA measurements. M.E. ILGAZI and S. BASIT performed the mechanical tests. M.E. ILGAZI and S. BASIT performed the corrosion tests. M.E. ILGAZI, I.MUTLU, S. BASIT, E. BALCI, and F. DAGDELEN analyzed the data and wrote the manuscript.

Data availability The data that support the findings of this study are available from the corresponding author upon reasonable request.

Declarations

Conflict of interest The authors state no conflict of interest in printing this manuscript.

References

1. Liu H, Zhao X, Yue Q, Gu Y. Microstructure and deformation mechanism of Ni-based wrought superalloys for A-USC power plants: a review. J Mater Sci. 2024;59(11):4404–30. https://doi.org/10.1007/s10853-024-09517-4.
2. Kvapilova M, Kral P, Dvorak J, Sklenicka V. High temperature creep behaviour of cast nickel-based superalloys INC 713 LC, B1914 and MAR-M247. Metals. 2021;11(1):152. https://doi.org/10.3390/met11010152.
3. Rathi N, Kumar P, Gupta A. Non-conventional machining of nickel based superalloys: a review. Mater Today Proc. 2023. https://doi.org/10.1016/j.matpr.2023.02.176.
4. Shahwaz M, Nath P, Sen I. Recent advances in additive manufacturing technologies for Ni-based Inconel superalloys – a comprehensive review. J Alloys Compd. 2024;1010:177654. https://doi.org/10.1016/j.jallcom.2024.177654.
5. Teng Q, Xie Y, Sun S, Xue P, Wei Q. Understanding on processing temperature–metallographic microstructure–tensile property relationships of third-generation nickel-based superalloy WZ-A3 prepared by hot isostatic pressing. J Alloys Compd. 2022;909:164668. https://doi.org/10.1016/j.jallcom.2022.164668.
6. Wang X, Gong X, Chou K. Review on powder-bed laser additive manufacturing of Inconel 718 parts. Proc Inst Mech Eng B J Eng Manuf. 2017;231(11):1890–903. https://doi.org/10.1177/0954405415619883.
7. Sonar T, Balasubramanian V, Malarvizhi S, Venkateswaran T, Sivakumar D. An overview on welding of Inconel 718 alloy – effect of welding processes on microstructural evolution and mechanical properties of joints. Mater Charact. 2021;174:110997. https://doi.org/10.1016/j.matchar.2021.110997.
8. Chen J, Chen J, Li S, Wang Y, Wang Q, Wu Y, et al. Enhanced creep resistance induced by minor Ti additions to a second generation nickel-based single crystal superalloy. Acta Mater. 2022;232:117938. https://doi.org/10.1016/j.actamat.2022.117938.
9. MacKay RA, Gabb TP, Garg A, Rogers RB, Nathal MV. Influence of composition on microstructural parameters of single crystal nickel-base superalloys. Mater Charact. 2012;70:83–100. https://doi.org/10.1016/j.matchar.2012.05.001.
10. Wang J, Wang L, Li J, Chen C, Yang S, Li X. Effects of aluminum and titanium additions on the formation of nonmetallic inclusions in nickel-based superalloys. J Alloys Compd. 2022;906:164281. https://doi.org/10.1016/j.jallcom.2022.164281.
11. Hosseini E, Popovich VA. A review of mechanical properties of additively manufactured Inconel 718. Addit Manuf. 2019;30:100877. https://doi.org/10.1016/j.addma.2019.100877.
12. Shahwaz M, Nath P, Sen I. A critical review on the microstructure and mechanical properties correlation of additively manufactured nickel-based superalloys. J Alloys Compd. 2022;907:164530. https://doi.org/10.1016/j.jallcom.2022.164530.
13. Chyrkin A, Gunduz KO, Fedorova I, Sattari M, Visibile A, Halvarsson M, et al. High-temperature oxidation behavior of additively manufactured IN625: effect of microstructure and grain size. Corros Sci. 2022;205:110382. https://doi.org/10.1016/j.corsci.2022.110382.
14. Jahangiri MR, Arabi H, Boutorabi SMA. Development of wrought precipitation strengthened IN939 superalloy. Mater Sci Technol. 2012;28(12):1470–8. https://doi.org/10.1179/174328471 2Y.0000000073.
15. Marchese G, Parizia S, Saboori A, Manfredi D, Lombardi M, Fino P, et al. The influence of the process parameters on the densification and microstructure development of laser powder bed fused Inconel 939. Metals. 2020;10(7):882. https://doi.org/10.3390/met10070882.
16. Yin Q, Liu Z, Wang B, Song Q, Cai Y. Recent progress of machinability and surface integrity for mechanical machining Inconel 718: a review. Int J Adv Manuf Technol. 2020;109:215–45. https://doi.org/10.1007/s00170-020-05665-4.
17. Volpato GM, Tetzlaff U, Fredel MC. A comprehensive literature review on laser powder bed fusion of Inconel superalloys. Addit Manuf. 2022;55:102871. https://doi.org/10.1016/j.addma.2022.102871.
18. Ajay P, Dabhade VV. Heat treatments of Inconel 718 nickel-based superalloy: a review. Metals Mater Int. 2024;31:1204–31. https://doi.org/10.1007/s12540-024-01812-8.
19. Qi H, Azer M, Ritter A. Studies of standard heat treatment effects on microstructure and mechanical properties of laser net shape manufactured Inconel 718. Metall Mater Trans A. 2009;40:2410–22. https://doi.org/10.1007/s11661-009-9949-3.
20. Muthu S, Arivarasu M. Investigations of hot corrosion resistance of HVOF coated Fe-based superalloy A-286 in simulated gas turbine environment. Eng Fail Anal. 2020;107:104224. https://doi.org/10.1016/j.engfailanal.2019.104224.
21. Osoba L, Oladoye A, Ogbonna V. Corrosion evaluation of superalloys Haynes 282 and Inconel 718 in hydrochloric acid. J Alloys Compd. 2019;804:376–84. https://doi.org/10.1016/j.jallcom.2019.06.196.
22. Selvaraj SK, Sundaramali G, Dev SJ, Swathish RS, Karthikeyan R, Vishaal KE, et al. Recent advancements in the field of Ni-based superalloys. Adv Mater Sci Eng. 2021;2021:9723450. https://doi.org/10.1155/2021/9723450.
23. Kanyo JE, Schafföner S, Uwanyuze RS, Leary KS. An overview of ceramic molds for investment casting of nickel superalloys. J Eur Ceram Soc. 2020;40(15):4955–73. https://doi.org/10.1016/j.jeurceramsoc.2020.07.013.
24. Markanday JFS. Applications of alloy design to cracking resistance of additively manufactured Ni-based alloys. Mater Sci Technol. 2022;38(16):1300–14. https://doi.org/10.1080/02670836.2022.2068759.
25. Dai S, Zhu J, Yan X, Wu S, Liu Y, Gao X, et al. Unique yttria nanoparticle strengthening in an Inconel 718 superalloy fabricated by additive manufacturing. Adv Mater Technol. 2024;9(3):2301421. https://doi.org/10.1002/admt.202301421.
26. Kunz L, Sklenicka V, Svoboda M, Kral P. Casting defects and high temperature fatigue life of IN 713LC superalloy. Mater Sci Eng A. 2012;41:47–51. https://doi.org/10.1016/j.ijfatigue.2011.12.002.
27. Li Y, Zhang J, Wang L, et al. Review on additive manufacturing of single-crystal nickel-based superalloys. Addit Manuf Lett. 2022;1(1):100019. https://doi.org/10.1016/j.amle.2021.100019.
28. Kipouros G, et al. On the advantages of using powder metallurgy in new light metal alloy design. Metall Mater Trans A. 2006;37:3429–36. https://doi.org/10.1007/s11661-006-1037-3.
29. Wang Z, et al. Powder metallurgy of titanium alloys: a brief review. J Alloys Compd. 2023;965:171030. https://doi.org/10.1016/j.jallcom.2023.171030.
30. Zhang S, et al. Microstructure characterization of a high strength Ti–6Al–4V alloy prepared from a powder mixture of TiH_2 and 60Al40V masteralloy powders. J Alloys Compd. 2020;818:152815. https://doi.org/10.1016/j.jallcom.2019.152815.
31. Higashi M, et al. Effect of initial powder particle size on the hot workability of powder metallurgy Ni-based superalloys. J Mater

Process Technol. 2020;194:108926. https://doi.org/10.1016/j.jmatprotec.2020.108926.
32. Shao YL, et al. Effect of Ti and Al on microstructure and partitioning behavior of alloying elements in Ni-based powder metallurgy superalloys. Trans Nonferrous Met Soc China. 2019;26:500–6. https://doi.org/10.1016/S1003-6326(19)64963-8.
33. Cheng S, et al. Microstructure, thermal stability and tensile properties of a Ni–Fe–Cr based superalloy with different Fe contents. Intermetallics. 2023;153:107785. https://doi.org/10.1016/j.intermet.2023.107785.
34. Bassini E, Marchese G, Aversa A. Tailoring of the microstructure of laser powder bed fused Inconel 718 using solution annealing and aging treatments. Metals. 2021;11(6):921. https://doi.org/10.3390/met11060921.
35. Tang C, et al. Nickel base superalloy GH4049 prepared by powder metallurgy. J Alloys Compd. 2009;474(1–2):201–5. https://doi.org/10.1016/j.jallcom.2008.06.095.
36. Liu W, Li L, Mi G, Wang J, Pan Y. Effect of Fe content on microstructure and properties of laser cladding Inconel 625 alloy. Materials. 2022;15(22):8200. https://doi.org/10.3390/ma15228200.
37. Tuzi S. Electron microscopy of oxide formed on nickel alloy X-750 in simulated boiling water reactor environment. PhD thesis. Chalmers University of Technology; 2017.
38. Calandri M, Yin S, Aldwell B, Calignano F, Lupoi R, Ugues D. Texture and microstructural features at different length scales in Inconel 718 produced by selective laser melting. Materials. 2019;12(8):1293. https://doi.org/10.3390/ma12081293.
39. Dagdelen F, Ercan E. The surface oxidation behavior of Ni–45.16% Ti shape memory alloys at different temperatures. J Therm Anal Calorim. 2014;115:561–5. https://doi.org/10.1007/s10973-013-3208-y.
40. Dong E, Yu W, Cai Q, Cheng L, Shi J. High-temperature oxidation kinetics and behavior of Ti–6Al–4V alloy. Oxid Met. 2017;88:719–32. https://doi.org/10.1007/s11085-017-9770-0.
41. Balci E, Somunkiran I, Ercan E, Dagdelen F, Aydogdu Y. A study on isothermal oxidation kinetics using thermogravimetric method of TiNiNb shape memory alloys. J Therm Anal Calorim. 2023;148(24):14253–60. https://doi.org/10.1007/s10973-023-12587-2.
42. Bucciarelli F, Malfense Fierro GP, Zarrelli M, Meo M. A nondestructive method for evaluation of the out of plane elastic modulus of porous and composite materials. Appl Compos Mater. 2019;26:871–96. https://doi.org/10.1007/s10443-018-9754-5.
43. de Souza IFM, Riffel KC, Paes LES, Franco SD, da Silva LRR. Welding and additive manufacturing challenges in nickel superalloys: the impact of hydrogen embrittlement. Processes. 2024;13(1):33. https://doi.org/10.3390/pr13010033.
44. Lim B, Chen H, Chen Z, Haghdadi N, Liao X, Primig S, et al. Microstructure-property gradients in Ni-based superalloy (Inconel 738) additively manufactured via electron beam powder bed fusion. Addit Manuf. 2021;46:102121. https://doi.org/10.1016/j.addma.2021.102121.
45. Ratia V, Miettunen I, Kuokkala VT. Surface deformation of steels in impact-abrasion: the effect of sample angle and test duration. Wear. 2013;301(1–2):94–101. https://doi.org/10.1016/j.wear.2013.01.006.
46. Franco AR, Sanchez Caceres JA, et al. Study of the erosive-abrasive wear resistance of Fe-14% Cr-2.8% C high chromium cast iron. Mater Res. 2024;27:e20230242. https://doi.org/10.1590/1980-5373-MR-2023-0242.
47. Panagopoulos C, Giannakopoulos K, et al. Wear behavior of nickel superalloy CMSX-186. Wear. 2003;57(29):4611–6.
48. Bearden JA, Burr AF. Reevaluation of X-ray atomic energy levels. Rev Mod Phys. 1967;39(1):125. https://doi.org/10.1103/RevModPhys.39.125.
49. Bakonyi I, et al. Accounting for the resistivity contribution of grain boundaries in metals: critical analysis of reported experimental and theoretical data for Ni and Cu. Prog Mater Sci. 2021;136:410. https://doi.org/10.1016/j.pmatsci.2022.101041.
50. Bardeen J, et al. Electrical conductivity of metals. Phys Rev. 1940;11(2):88–111. https://doi.org/10.1103/PhysRev.58.727.
51. Mu S, et al. Uncovering electron scattering mechanisms in NiFeCoCrMn derived concentrated solid solution and high entropy alloys. npj Comput Mater. 2019;5(1):1. https://doi.org/10.1038/s41524-019-0178-1.
52. Cai J, et al. Characterizing short-time aging precipitation behavior of a novel nickel–iron-based alloy via electrical performance. Materials (Basel). 2024;17(16):4143. https://doi.org/10.3390/ma17164143.
53. Pereira D, et al. Effect of microstructure on electrical conductivity of Inconel 718 alloys. Mater Sci Eng A. 2015;31(6):669–76. https://doi.org/10.1016/j.msea.2015.02.034.
54. Nagarajan B, et al. Influence of heat treatment on the conductivity of nickel-based superalloys. MATEC Web Conf. 2015. https://doi.org/10.1051/matecconf/20151304002.
55. Nagarajan B, et al. Effect of microstructure on electrical conductivity of nickel-base superalloys. Metall Mater Trans A. 2017;48(8):3745–57. https://doi.org/10.1007/s11661-017-4104-3.
56. Shahzad K, Sliem MH, Shakoor RA, Radwan AB, Kahraman R, Umer MA, et al. Electrochemical and thermodynamic study on the corrosion performance of API X120 steel in 3.5% NaCl solution. Sci Rep. 2020;10(1):4314. https://doi.org/10.1038/s41598-020-61139-3.
57. Balci E, Dagdelen F, Qader IN, Mohammed SS, Aydogdu Y. Investigation of bio-corrosion behavior, structural and thermal properties of Ni20Ti50Sn30 high-temperature shape memory alloy. J Therm Anal Calorim. 2024;149(17):9085–93. https://doi.org/10.1007/s10973-024-13376-1.
58. Thuneman T, Raja KS, Charit I. Room temperature corrosion behavior of selective laser melting (SLM)-processed Ni-Fe superalloy (Inconel 718) in 3.5% NaCl solution at different pH conditions: role of microstructures. Crystals. 2024;14(1):89. https://doi.org/10.3390/cryst14010089.
59. Benaioun N, Moulayat N, Hakiki NE, Ramdane H, Denys E, Florentin A, et al. Passive films formed on Fe- and Ni-based alloys in an alkaline medium: an insight into complementarities between electrochemical techniques and near-field microscopies (AFM/SKPFM). Appl Sci. 2023;13(21):11659. https://doi.org/10.3390/app132111659.
60. Tuzi S, Stiller K, Thuvander M. Oxidation of Alloy X-750 with low iron content in simulated BWR environment. J Nucl Eng. 2023;4(4):711–22. https://doi.org/10.3390/jne4040044.
61. Tuzi S, Göransson K, Rahman SMH, Eriksson SG, Liu F, Thuvander M, et al. Oxide evolution on Alloy X-750 in simulated BWR environment. J Nucl Mater. 2016;482:19–27. https://doi.org/10.1016/j.jnucmat.2016.09.026.